

Article

Superlattice Symmetries Reveal Electronic Topological Transition in CaC₆ with Pressure

Bruce Wang^{1,2}, Antonio Bianconi³ , Ian D. R. Mackinnon⁴  and Jose A. Alarco^{1,2,4,*} 

- ¹ School of Chemistry and Physics, Queensland University of Technology, Brisbane, QLD 4001, Australia; p44.wang@qut.edu.au
- ² Centre for Materials Science, Queensland University of Technology, Brisbane, QLD 4001, Australia
- ³ Rome International Center for Materials Science Superstripes (RICMASS), Via dei Sabelli 119A, 00185 Roma, Italy; antonio.bianconi@ricmass.eu
- ⁴ Centre for Clean Energy Technologies and Practices, Queensland University of Technology, Brisbane, QLD 4001, Australia; ian.mackinnon@qut.edu.au
- * Correspondence: jose.alarco@qut.edu.au

Abstract: The electronic properties of calcium-intercalated graphite (CaC₆) as a function of pressure are revisited using density functional theory (DFT). The electronic band structures of CaC₆, like many other layered superconducting materials, display cosine-shaped bands at or near the Fermi level (FL). Such bands encompass bonding/antibonding information with a strong connection to superconducting properties. Using a hexagonal cell representation for CaC₆, the construction of a double supercell in the *c*-direction effects six-folding in the reciprocal space of the full cosine function, explicitly revealing the bonding/antibonding relationship divide at the cosine midpoint. Similarly, folding of the Fermi surface (FS) reveals physical phenomena relevant to electronic topological transitions (ETTs) with the application of pressure. The ETT is characterised by a transition of open FS loops to closed loops as a function of pressure. As the highest transition temperature is reached with pressure, the dominant continuous, open FS loops shift to a different region of the FS. For CaC₆, the peak value for the superconducting transition temperature, T_c, occurs at about 7.5 GPa, near the observed pressure of the calculated ETT. At this pressure, the radius of the nearly spherical Ca 4s-orbital FS coincides with three times the distance from the Γ centre point to the Brillouin zone (BZ) boundary of the 2*c* supercell. In addition, the ETT coincides with the alignment of the nonbonding (inflection) point of the cosine band with the FL. At other calculated pressure conditions, the Ca 4s-orbital FS undergoes topological changes that correspond and can be correlated with experimentally determined changes in T_c. The ETT is a key mechanism that circumscribes the known significant drop in T_c for CaC₆ as a function of increasing pressure. Consistent calculated responses of the ETT to pressure match experimental measurements and validate the examination of superlattices as important criteria for understanding mechanisms driving superconductivity.



Citation: Wang, B.; Bianconi, A.; Mackinnon, I.D.R.; Alarco, J.A. Superlattice Symmetries Reveal Electronic Topological Transition in CaC₆ with Pressure. *Crystals* **2024**, *14*, 554. <https://doi.org/10.3390/cryst14060554>

Academic Editor: Artem Pronin

Received: 22 May 2024

Revised: 9 June 2024

Accepted: 11 June 2024

Published: 14 June 2024

Keywords: superconductivity; CaC₆; Fermi surface; Fermi level; electronic topological transition; superlattice



Copyright: © 2024 by the authors. Licensee MDPI, Basel, Switzerland. This article is an open access article distributed under the terms and conditions of the Creative Commons Attribution (CC BY) license (<https://creativecommons.org/licenses/by/4.0/>).

1. Introduction

Graphite intercalant compounds (GICs) are among the many interesting carbon (C)-containing families of superconductors [1–3]. Superconductivity was discovered in the compound calcium-intercalated graphite (CaC₆) in 2005, exhibiting a critical temperature (T_c) of 11.5 K at ambient pressure [4]. In this compound, calcium (Ca) is intercalated between graphene layers. Initially, there was ambiguity regarding the number of graphene layers and Ca stacking in the primitive unit cells, as CaC₆ was first believed to adopt a hexagonal structure with double layers [5], similar to other metal-intercalated graphite compounds like YbC₆ (which has a T_c of 6.5 K) [4]. This misconception was clarified through the synthesis of bulk CaC₆ [6], which confirmed a distinctive rhombohedral

symmetry ($R\bar{3}m$) compared to other GICs. This discovery of T_c in CaC_6 , coupled with the aspiration to broaden the applications of graphene, ignited substantial research interest that yielded several pivotal findings [7–9].

The understanding of superconductivity in CaC_6 has been the subject of ongoing debate among researchers. In 2005, Csányi et al. investigated the influence of the free-electron-like interlayer states on the superconductivity of GICs, including YbC_6 and CaC_6 , using density functional theory (DFT) [10]. They hypothesised that a weak coupling between the interlayer states and the graphene layers in GICs creates conditions favourable for soft charge fluctuations. Such conditions could, in turn, foster s-wave superconductivity via an excitonic pairing mechanism. Mazin [5], using DFT calculations, postulated a different origin for superconductivity in YbC_6 and CaC_6 . Mazin proposed a different mechanism involving vibrations from the intercalating elements with the dominant role of the intercalant electronic states at the Fermi level (FL), leading to a pronounced coupling with soft intercalant modes. However, it should be highlighted that both Csányi and Mazin overlooked the correct symmetry of CaC_6 in their analyses.

Weller, in 2005 [4], stressed the absence of a direct correlation between the amount of charge transferred and T_c . He speculated that the superconductivity evident in GICs could be associated with a resonant valence bond mechanism. A thorough first-principles electron–phonon coupling study was carried out on CaC_6 by Calandra et al. [11]. Employing the McMillan formula [12], the critical temperature was computed by Calandra et al. [11], aligning well with experimental data. Notably, the calculated isotope effect for Ca stood at 0.24 K. This value contrasts with the experimental observation of a large isotope effect, with about a 0.5 K shift in T_c for Ca reported by Hinks et al. [13].

Additionally, Hinks et al. [13] highlighted the differences in charge transfer between the two compounds CaC_6 and MgB_2 . In MgB_2 , complete charge transfer from magnesium to the boron network results in strong coupling between carriers and high-energy in-plane boron vibrations, leading to high- T_c superconductivity. However, in CaC_6 , charge transfer is incomplete, leading to the presence of an interlayer band at the FL. This interlayer band couples with calcium phonons, and this interaction is believed to be responsible for the relatively high T_c observed in CaC_6 . The precise details of this interaction and its contribution to the observed T_c are still not fully understood. The discrepancy for the Ca isotope effect suggests that the electron–phonon mechanism alone might not fully account for the superconducting attributes of CaC_6 [13].

Subsequent experimental investigations have yielded further evidence elucidating the superconductivity mechanism in CaC_6 . A landmark study by G. Lamura [14] marked the first measurement of the magnetic penetration depth in bulk CaC_6 , revealing a depth of 720 ± 80 Å. Lamura emphasised that a single-gap analysis aptly captures the data with minimal determination error. He attributed the pairing to the interaction between Ca s-band electrons and the phonon modes of both C out-of-plane and Ca in-plane. Further validation of the s-wave superconducting gap came from scanning tunnelling spectroscopy [15]. Both DFT calculations [16] and directional point-contact spectroscopy [17] identified an anisotropic gap, noting values of 1.35 meV and 1.71 meV, respectively. The inconsistency among experimental observations, as well as between theoretical predictions and experimental findings concerning the superconducting properties of CaC_6 , highlights the necessity for further in-depth investigation.

Like isotopic effects, understanding pressure effects on the superconducting properties of CaC_6 can also provide insights into the underlying mechanisms. Smith et al. [18] investigated the pressure dependence of T_c for CaC_6 and YbC_6 up to 1.2 GPa. CaC_6 exhibited a linear T_c increase with pressure, while YbC_6 's T_c initially rose, peaked, and then declined. In a subsequent experiment [19], the T_c of superconducting CaC_6 displayed a prominent linear rise with pressure, reaching 15.1 K at 7.5 GPa. However, at 8 GPa, a shift to a new phase was noted, characterised by a diminished T_c and inferior metallic properties at room temperature. This phenomenon is believed to be due to pressure-induced phonon softening linked to an in-plane Ca phonon mode. Separately, Gauzzi et al. [20] analysed the

room-temperature crystal structure of bulk CaC_6 under pressures up to 13 GPa. At 9 GPa, they identified an order–disorder transition coupled with lattice softening. Contrary to expectations of symmetry reduction, the CaC_6 structure favoured a disordered arrangement of intercalant Ca atoms in the a – b plane. While the $R\bar{3}m$ space-group symmetry remained unchanged, there was a significant rise in isothermal compressibility and a pronounced broadening of Bragg peaks.

The Fermi surface (FS)-dependent superconducting gap and electron–phonon coupling in CaC_6 were studied by Sugawara et al. [21] and Valla and Pan [22] using Angle-Resolved Photoemission (ARPES). They discovered that the superconducting gap is anisotropic and varies depending on the FS and provided insights into the electron–phonon coupling in the compound. Yang et al. [23] provided further insight into the superconducting mechanism of CaC_6 using ARPES, emphasising the critical role of the interaction between the π^* antibonding orbitals and interlayer bands. Their analysis of superconducting gaps and electron–phonon coupling strengths highlighted the importance of these parameters in achieving the superconducting phase transition. Additionally, they suggested the possibility of inducing superconductivity in a monolayer of graphene by creating an adatom superlattice. Theoretical investigations also extended beyond the superconductivity of CaC_6 . Rahnejat et al. [24] observed a charge density wave (CDW) in CaC_6 using ARPES, which did not cause any distortion of the carbon nuclei, highlighting the remarkable rigidity of graphene. This finding suggested the possibility of inducing a CDW and even superconductivity in a graphene-based field-effect transistor through electron-doping.

The geometrical and topological aspects of superconductivity, in both real and reciprocal spaces, are currently topical and gaining widespread interest from the research community. Topology helps to understand not only the details of the physical phenomena but also some general regularity connecting physical behaviours [25]. Topological properties are relevant for quantum materials, which include superconductors, graphene, topological insulators, Weyl semimetals, quantum spin liquids, and spintronic devices, among others [26]. Topology contributes to the scientific search for universality, assisting in the identification of underlying organising principles and the evaluation of concepts that can be developed to enable a deeper understanding [27].

In this work, using first-principles calculations, we systematically investigate changes in the topologies of the electronic band structures (EBSs) and FSs of CaC_6 under various pressures. We evaluate two software versions of DFT and benchmark specific computational parameters in order to determine, at the meV scale, details of the EBS and FS variation with pressure. The pressure-driven alterations in EBSs, FSs, and electronic charge are analysed in terms of a double superlattice cell along the c -axis using a hexagonal lattice with Space Group P1. The information derived in this article by using superlattices further validates their introduction and is complementary to the information provided in a companion article [28].

In CaC_6 , bands at or near the FL show a cosine-modulated dependence. This dependence implies a bonding/antibonding (or in-phase/out-of-phase) modulation, as noted in earlier work [28,29]. Superlattices, when identified, appropriately incorporate this phase information inherent in electronic band structures (EBSs), as described in the companion article [28]. The interpretation of results from a superlattice perspective identifies an electronic topological transition (ETT), consistent with the well-established understanding of the ETTs of other layered and non-layered superconductors. Without a superlattice construct, the ETT and relevant mechanistic information for superconductivity, extractable from the EBS, remains hidden and undetected. The findings provide fresh insight into the principles driving superconductivity in CaC_6 , thereby enriching our understanding of superconducting properties.

2. Methods

We conducted a comprehensive DFT analysis of the EBSs and FSs of CaC₆ within a pressure range from 0 GPa up to 16 GPa using Quantum ESPRESSO Version QE-7.3 [30] and Materials Studio CASTEP 2023 [31] for comparison. Crystal structures are visualised with Crystal Maker V11.0.2 using geometry-optimised cell parameters of experimentally determined values.

Due to the small superconducting gap for CaC₆ (~1.7 meV), achieving convergence that accurately predicts ground-state properties is essential. Previous studies have indicated the feasibility of deducing critical temperatures from electronic band structures under higher-convergence conditions [32–34]. Considering the necessity for high precision in determining the superconducting gap, to an accuracy of about 10^{−1} meV, we implemented a meticulous benchmarking process, with the detailed results provided in the Supporting File. This process entailed a thorough evaluation of parameters, including plane-wave cut-off energies, pseudopotentials, and k-point grids [32]. We provide the details of this evaluation in the Supplemental Materials.

Our benchmarking tests varied cut-off energies from 40 Ry (=544 eV) to 200 Ry (=2720 eV) and showed that low cut-off energies lead to large deviations from consistent results. As shown in Figure S2 (Supplemental Materials), we observed that the total energy of CaC₆ converges within a margin of 1 meV for cut-off energies higher than 120 Ry. Additionally, fluctuations in Fermi energies (FEs), with a consistent magnitude of ~0.2 meV, were only noted when cut-off energies exceeded 100 Ry. Given that Δ , the zero-temperature superconducting gap, is 1.79 ± 0.08 meV [17,21], selecting cut-off energies above 120 Ry was deemed appropriate for accurate representation.

Further, we evaluated the total system energies and Fermi surface of CaC₆ using a variety of k-point grids. The convergence behaviour for both the total energy and FE under different k-point grids is detailed in Figure S3 (Supplemental Materials). Our findings suggest that the total energy stabilises using k-point grids with a density higher than a $24 \times 24 \times 24$ sampling grid, with energy fluctuations ranging from −0.1 meV to 0.1 meV beyond this point. The FE demonstrated similar trends, achieving convergence with the $24 \times 24 \times 24$ k-point grid.

To select suitable pseudopotentials, we adopted a systematic approach, testing various options and comparing preliminary results with experimental data. In the context of CaC₆, a rhombohedral crystal structure has been experimentally determined [6]. The experimental X-ray diffraction data provide lattice constants: $a = 5.17$ and $\alpha = 49.55^\circ$. These lattice parameters are converted to an equivalent centrosymmetric hexagonal cell with D_{3d} Schoenflies point-group symmetry for EBS calculations.

To assess and optimise the choice of pseudopotentials, we performed unit cell relaxation using ten distinct pseudopotentials. The pseudopotentials include GGA + PAW, GGA + US, LDA + PAW, LDA + US, GGA + US + rVV10 [35], GGA + US + vdW-DF [36,37], GGA + US + vdW-DF2 [38], GGA + US + vdW-DF3-opt1 [39], GGA + US + vdW-DF3-opt2 [39], and GGA + US + vdW-DF-C6 [40]. These pseudopotentials encompass a range of exchange-correlation approximations and treatments of electron–electron interactions, including van der Waal (vdW) interactions [41]. We evaluate these pseudopotentials in order to comprehensively investigate their influence on the calculated properties.

By employing this comprehensive array of pseudopotentials and drawing comparisons with experimentally determined lattice constants and other pertinent properties, we aim to identify the pseudopotential that best aligns with the observed behaviour of CaC₆, ultimately enhancing the accuracy and reliability of our computational predictions. Figure S4 (Supplemental Materials) indicates the disparities between simulated lattice parameters and corresponding experimental data for the various pseudopotentials noted above. The chart offers insight into the accuracy of different pseudopotentials in reproducing experimental lattice parameters (assumed to be measured at low temperature, although the temperature conditions of the experimental XRD analysis are not disclosed [6]) and follows earlier investigations on pseudopotential choices for MB₂- and MB₆-type compounds [42–44].

As shown in Figure S4 (Supplemental Materials), simulations using GGA + PAW, GGA + US, and GGA + US + rVV10 pseudopotentials yield the lattice parameter values that most closely approximate experimental values. While all three options display promising alignment with experimental data, considerations of computational efficiency became pivotal in the selection process. For simulations employing the GGA + US pseudopotential, the discrepancies in lattice parameters compared to experimental data stand at 0.19% for a and 0.46% for α . These small deviations underscore the reliability of the chosen pseudopotential and its capacity to represent the properties of CaC_6 .

Following these benchmarking calculations, we chose to employ ultrasoft pseudopotentials [45] with a generalised gradient approximation (GGA) [46,47] for the exchange-correlation functional based on the closest match between reported calculated and experimental lattice parameters. Eigenfunctions were expanded using a plane-wave basis set with a cut-off energy of 120 Ry. For the wavefunctions and density of states, we used a $24 \times 24 \times 24$ Monkhorst–Pack grid [48] and a 0.02 Ry Methfessel–Vanderbilt smearing [49]. We also explored norm-conserving pseudopotentials within the LDA and GGA approximations using CASTEP with a cut-off energy of 990 eV and Δk -grid of 0.005 \AA^{-1} for additional comparisons.

For CaC_6 , based on the atomic position symmetry, it is generally accepted that a rhombohedral structure applies with the lattice parameters $a_R = 0.517 \text{ nm}$ and $\alpha = 49.55^\circ$ and group symmetry $R\bar{3}m$ [28,50]. This structure can also be represented by an equivalent hexagonal structure with the lattice parameters $a = b = 0.433 \text{ nm}$, $\alpha = \beta = 90^\circ$, and $\gamma = 120^\circ$. In a rhombohedral view of CaC_6 , the calcium atoms are stacked along the c -axis in an $A\alpha A\beta A\gamma$ sequence. The AA stacking pattern represents two adjacent layers of graphene. In this structure, the intercalant metal atoms within each layer occupy one of three prismatic hexagonal sites, labelled as α , β , and γ . Following standard conventions [50] for high-symmetry paths, as depicted in Figure S5, the key symmetry directions ΓZ and ΓA are related as follows (see also ref. [28]):

$$\Gamma Z^R = 3\Gamma A^H \quad (1)$$

$$\Gamma Z^R = \pi/c. \quad (2)$$

$$c = 13.572A \quad (3)$$

$$(a_1^* + a_2^* + a_3^*)/3 = \pi/c \quad (4)$$

where a_1^* , a_2^* , and a_3^* represent the reciprocal unit-cell vectors in the rhombohedral lattice, while c denotes the hexagonal lattice spacing in the direction perpendicular to the graphene layers.

DFT calculations considered both a primitive rhombohedral unit cell and the equivalent hexagonal counterpart. The specific lattice constants used as input for calculations were taken from the X-ray diffraction results of bulk CaC_6 [6]. Figure 1 shows the schematics of the hexagonal structure after geometry optimisation for selected isostatic pressures. We have also explored several supercell calculations, which could lead to the folding of reciprocal space [28,29] in selected high-symmetry directions. Figure 2 shows a schematic of the $2c$ double hexagonal supercell. The supercell periods effectively track the bonding/antibonding modulations (or alternating phase changes) in reciprocal space, indicated by an electronic band with a cosine function near the FL [51].

Using a hexagonal cell with equivalent symmetry to the rhombohedral cell, the original cosine function, which runs along the direction perpendicular to the planes or layers, has a periodicity of the $2c$ -lattice parameter in real space [28]. By using a $2c$ supercell, the periodicity of a $1c$ -lattice folded at the midpoint is equivalent in reciprocal space and defines a new BZ boundary where the nonbonding condition is defined.

For the EBS of the supercell, two cosine branches exist: one with lower energy for the bonding condition and another with higher energy for the antibonding condition. These two branches intersect the Γ point at the maximum bonding (lowest) and maximum antibonding (highest) energy values. The periodicities of these phase modulations may

also originate from and correspond to atomic orbital symmetry, as noted in earlier work on MgB_2 [32].

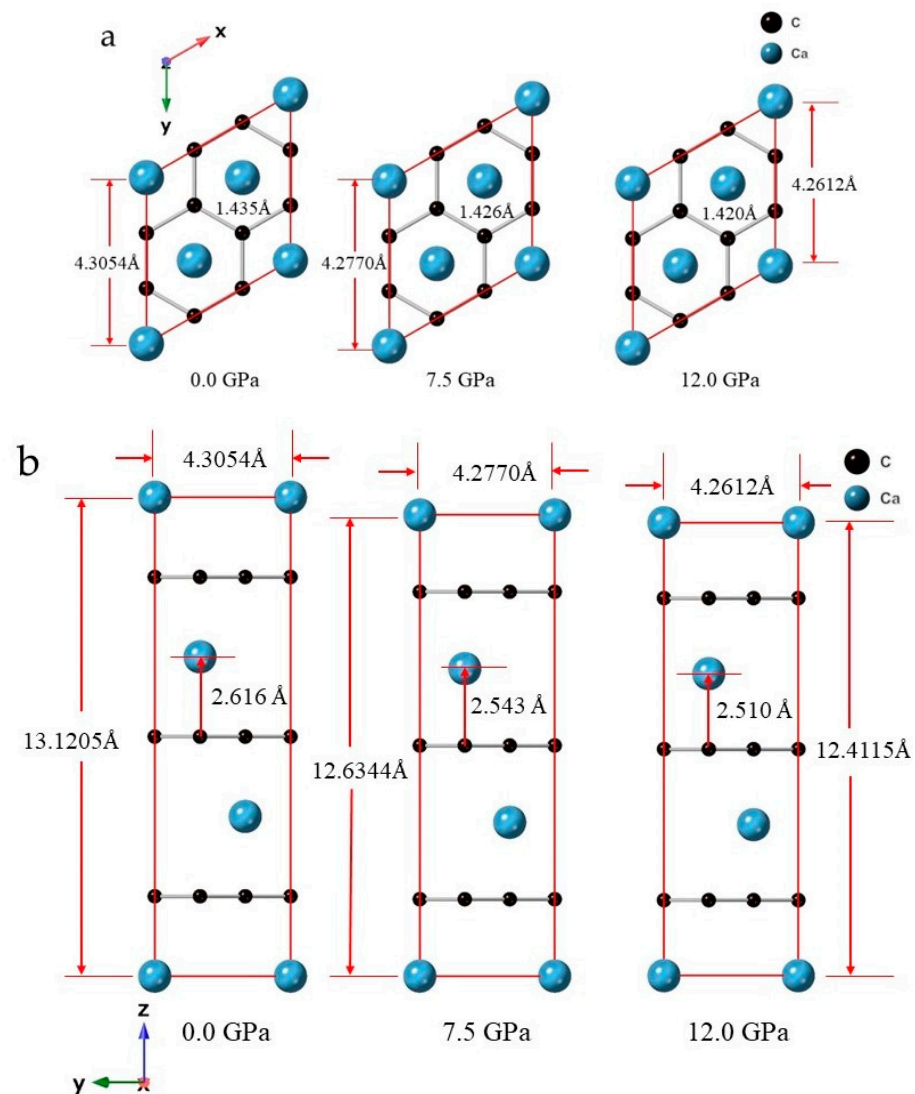


Figure 1. The crystal structure of CaC_6 using the $1c$ hexagonal cell representation for different pressures: 0 GPa, 7.5 GPa, and 12.0 GPa. (a) The top view along the c -, c^* -, or z -axis; (b) the view along one side of the basal plane of the hexagonal cell.

For clearer and deeper insight, we mapped the FSs under varying pressures, using FermiSurfer [52] to visualise the FSs from the Quantum ESPRESSO output data. Charge transfer data were calculated using the software Bader Charge Analysis v1.05 [53–56]. The CASTEP results on FSs were exported in bitmap format from their display in the software with a limited selection of FS branches and used for a complementary illustration of information.

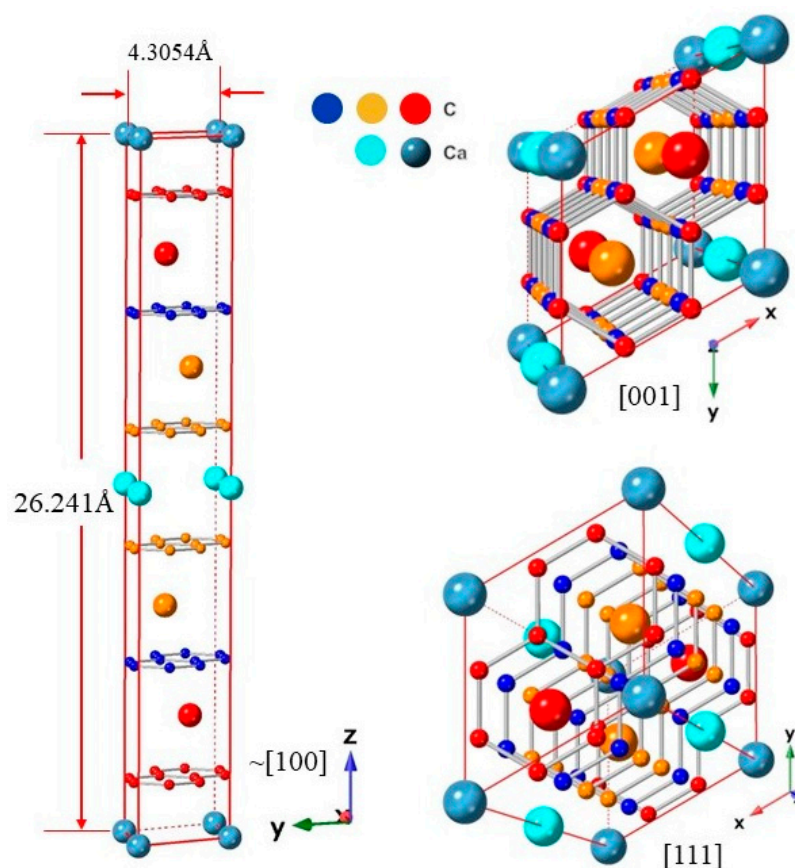


Figure 2. The crystal structure of CaC_6 using the $2c$ double hexagonal cell representation at 0 GPa pressure. Perspective views along directions $\sim[100]$, $[001]$, and $[111]$ are shown and labelled. Different colours for Ca and C are used to differentiate the layers in which the atoms reside within the $2c$ double supercell.

3. Results and Discussion

This section presents our findings from the DFT analysis of CaC_6 and is divided into three parts. We begin by looking at how the EBSs and FSs fold when double supercells are introduced. Then, we explore how EBSs and FSs change with different pressure levels and identify the ETT. Finally, we discuss the connection between the ETT, or Lifshitz transition, and the superconducting properties of CaC_6 . Through this approach, we shed light on factors that determine the superconducting behaviour of CaC_6 and identify further common features with ETTs for other superconductors.

3.1. Electronic Band Structures, Fermi Surfaces, and Superlattices

The DFT-calculated EBS and reciprocal path directions for the $2c$ double hexagonal unit cell are shown in Figure 3a,b, respectively. The equivalent results for the rhombohedral unit cell with high-symmetry paths, which follow the conventions described in reference [50], are given in Supplementary Figures S5 and S6 for convenience.

A nearly free electron band in the ΓZ reciprocal space direction, with a folded cosine-modulated shape for the $2c$ double hexagonal cell, can be observed crossing the FL (see the band and labelled regions inside the yellow box in Figure 3a). The midpoint of the cosine-modulated band is an inflection point at Z for the derivative of the band [29,57], separating folded regions with bonding and antibonding character, from Γ to Z and back from Z to Γ , respectively. Constructing a double superlattice along $2c$ in real space folds the reciprocal space in two at the Z point and folds the EBS, thus clearly highlighting the bonding and antibonding regions [29,57].

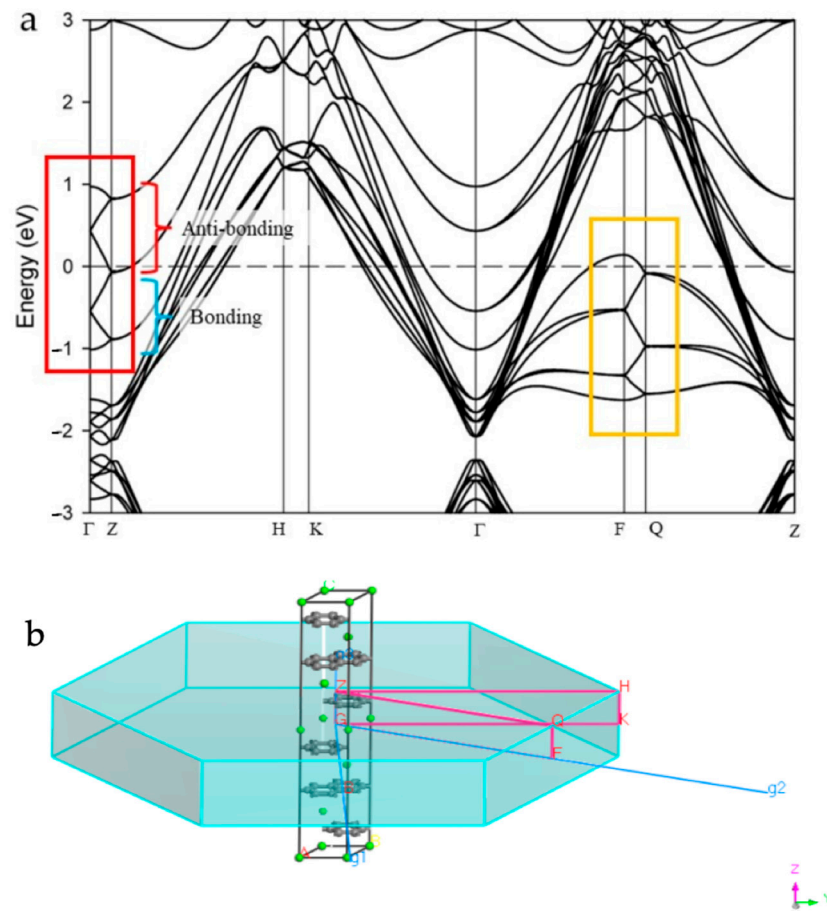


Figure 3. (a) The band structure and (b) reciprocal path directions for CaC_6 using a $2c$ double supercell. The red box encloses a folded version of the cosine-shaped band. Bonding/antibonding-character regions of the band are labelled. Intersections of the folded cosine-shaped bands with the Γ line correspond to the locally minimum bonding energy B or B' and locally maximum antibonding energy A or A'. Note that the approximate (folded) cosine shape is retained as the band moves along the a_2^* reciprocal axis (labelled g_2 in CASTEP) towards the zone boundary (as can be seen in the band along FQ enclosed in the orange box).

For the hexagonal cell shown in Figure 1a,b, the EBS is triply folded in the c^* -axis direction (see reference [28]), as expected from the relationship between the reciprocal space directions for rhombohedral and hexagonal unit cells given in Equations (1)–(4). A double hexagonal supercell has the correct $2c$ -lattice dimension that locates the required folding at the midpoint of the original cosine function for the distinct separation of bonding and antibonding regions. From Supplemental Figure S6, which displays the projected energy bands and DOS for the primitive rhombohedral unit cell, we can see that the majority of electrons at the Fermi level have Ca 4s and C with $2p_z$ -orbital character. There is a small fractional contribution of electrons from C with 2s-orbital character, particularly for the cosine-shaped band.

Figure 4a,b show cross-sections of the FS of CaC_6 calculated for the $2c$ double hexagonal supercell at 0 GPa using CASTEP. In Figure 4a, an additional FS band compared to Figure 4b is shown with partial transparency. However, as the number of bands increases, it becomes more difficult to distinguish overlapping sections. Figure 4b shows a magnified view of the FS shown in Figure 4a but with one less FS band (notice that the circle arc in the equatorial, horizontal direction is missing in Figure 4b). On the other hand, the circular caps at the top and bottom of the FS, which are barely, if at all, visible in Figure 4a, are more clearly distinguishable in Figure 4b. This is one of the advantages of QE over CASTEP for

displaying multiple FSs, because cross-sections can be precisely cut at chosen planes, while CASTEP shows overlapping volumetric contours.

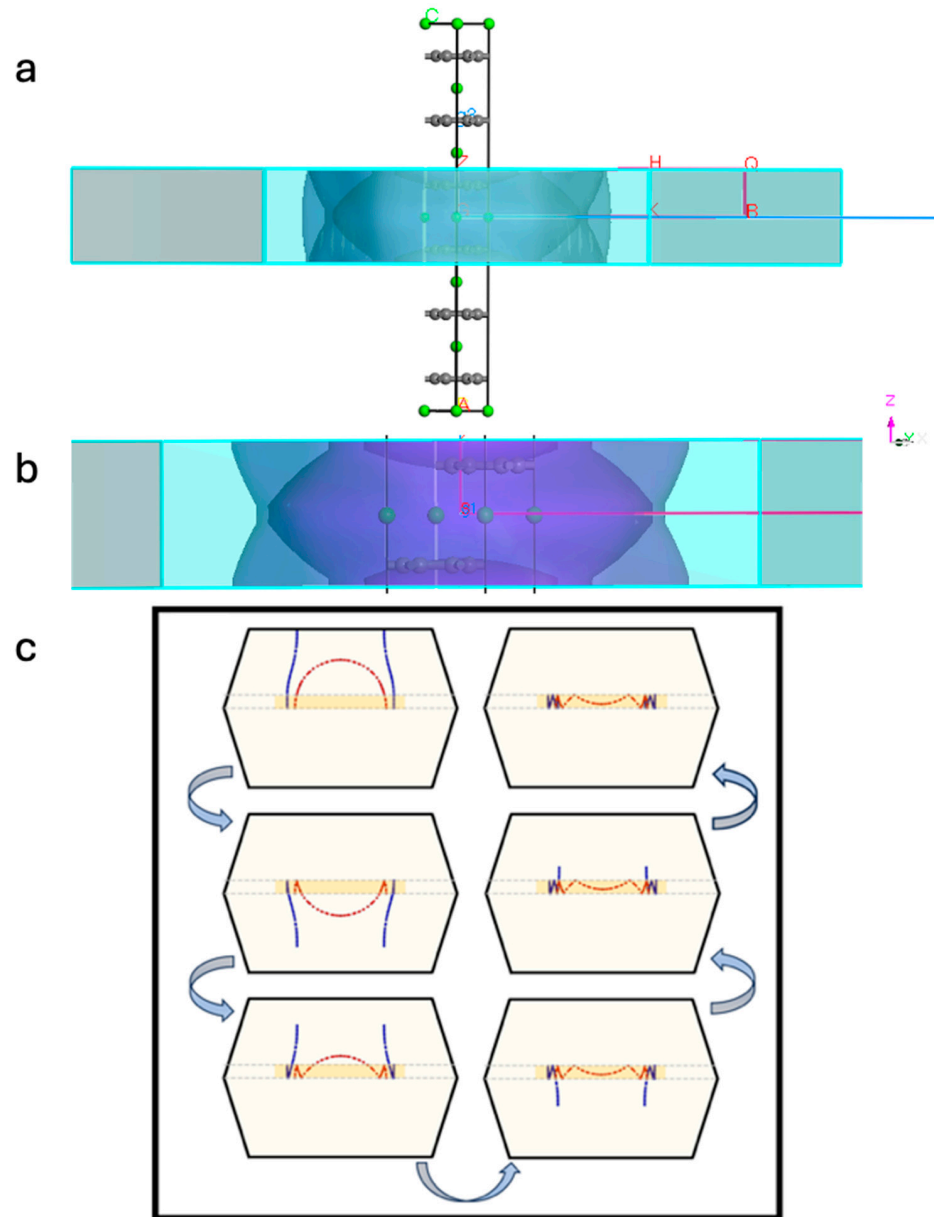


Figure 4. (a) A side view of the Fermi surface for the 2c double hexagonal superlattice, displaying a few selected FS bands, directly calculated using CASTEP. (b) An enlarged view of the FS in (a) displaying one less FS band; the top and bottom FS spherical caps become more apparent. (c) An illustration of folding in the cross-sectional view of the rhombohedral FS in the upper half of its BZ into 1/6 of the BZ corresponding to the double hexagonal supercell (see text for details).

Figure 4c shows the procedure of how the rhombohedral FS surface can be folded six times to obtain the 2c double hexagonal FS. Notice that for the FSs directly calculated for the 2c double superlattices, the intersections of the FSs with the BZ boundaries are perpendicular (see red circled regions in Figure 4b) and that adjacent FS branches at potential intersections develop gaps instead. These gaps are more clearly noticeable in CASTEP calculations because of the use of a much coarser grid (0.005 \AA^{-1}) compared to that used in QE (0.0015 \AA^{-1}).

3.2. Electronic Band Structures and Fermi Surfaces with Pressure

The folded, nearly free interlayer band crossing the FL (predominantly with Ca 4s-orbital character) shifts in position towards higher energy values with increasing pressure, as shown in Figure 5. The equivalent calculation results for rhombohedral unit cells are displayed in Supplemental Figure S8. Figures 5 and S8 demonstrate that the highest critical temperature (T_c) for CaC_6 is achieved when the interlayer band is half-filled, after which there is a notable decline as the band increases in energy. Similarly, the charge transfer from calcium to carbon in CaC_6 exhibits a comparable pattern, increasing with pressure, peaking around 7.5 GPa, and then decreasing thereafter (see Table 1).

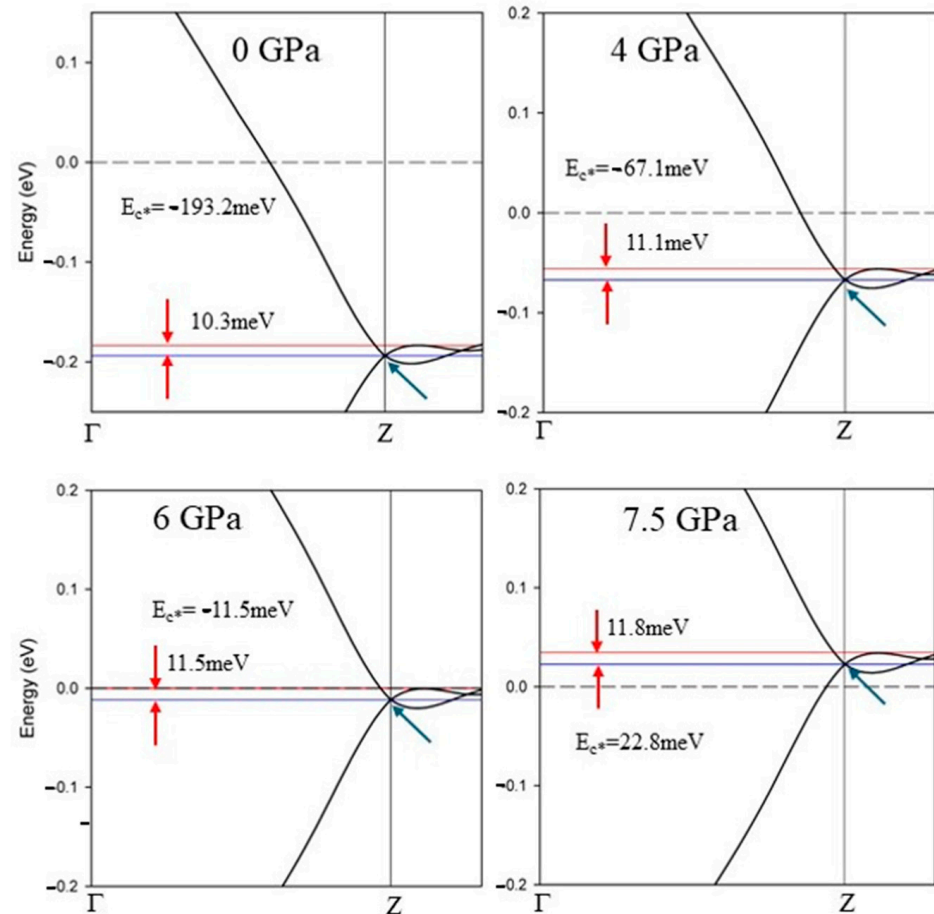


Figure 5. Folded sections of the electronic band structures of CaC_6 along the GZ direction for $2c$ double hexagonal supercells, presented as a function of pressure. The curve at 0 GPa is an enlarged view of Figure 3a. A comparison of EBSs with the same energy and reciprocal direction scale(s) for 0, 4, 6, and 7.5 GPa. Note the shift to higher energy (E_{c^*}) for the intersection of the antibonding and bonding bands (blue arrow) with the increase in pressure. The corresponding calculations for the primitive rhombohedral unit cell are shown in Supplementary Figure S8. The experimentally determined superconducting transition temperatures for the different pressures are given in green below the corresponding cosine-modulated bands in Figure S8.

The comprehensive properties of CaC_6 , including lattice constants, Fermi energy, $E_{\Gamma\frac{Z}{2}}$, and calculated charge transfer, are detailed in Table 1 (see also Supplemental Figure S10). In contrast to charge transfer, other properties of CaC_6 exhibit a more uniform trend. The values in Table 1 have been calculated using the rhombohedral group symmetry $R\bar{3}m$ and GGA + US pseudopotential, as described in the Section 2. α , β , and γ are the lattice constants of CaC_6 hR (rhombohedral unit cell), $E_{\Gamma\frac{Z}{2}}$ denotes energy levels at $\frac{\Gamma Z}{2}$ of interlayer bands, and the critical temperature T_c is adapted from reference [19]. Compare the values given in Table 1 of reference [28], which were calculated using a $2c$ hexagonal supercell and LDA pseudopotentials.

Table 1. Properties of CaC_6 under pressure.

Pressure (GPa)	a (Å)	α, β, γ (°)	$E_{\Gamma\frac{Z}{2}}$ (meV)	Fermi Energy (eV)	Charge Transferred from Ca to C	T_c (K)
0	5.1608	49.742	−312.413	9.7412	1.307427	11.4
2	5.0997	50.287	−279.467	10.0555	1.302507	12.6
4	5.0483	50.741	−122.392	10.1288	1.314594	13.6
6	5.0031	51.138	−45.043	10.295	1.315575	14.4
7	4.9823	51.321	−9.683	10.3734	1.314397	15
7.5	4.9724	51.408	7.662	10.4116	1.314443	15.1
8	4.9627	51.492	24.126	10.4489	1.314156	14.8
9	4.9439	51.656	129.716	10.5223	1.313847	11.2
10	4.9260	51.812	86.883	10.5933	1.313196	5.4
12	4.8930	52.105	144.067	10.7297	1.310696	4.8
16	4.8319	52.627	246.311	10.9836	1.306175	4.5

Figure 6 shows volumetric representations and cross-sections of the FS along the $\Gamma - Z - L$ plane as a function of pressure for the rhombohedral primitive unit cell (see also Figures 4, S7 and S8). The colour bar represents the relative value of the Fermi velocity of the electrons. For the rhombohedral unit cell, the apex of the FS of a predominant Ca 4s-orbital character (i.e., the top of the slightly distorted sphere) is clearly observed moving towards $\frac{\Gamma Z}{2}$ with increased pressure (see Figure 6e). The apex reaches $\frac{\Gamma Z}{2}$ at about 7.5 GPa and continues below $\frac{\Gamma Z}{2}$ at pressures equal to and above 8 GPa, which matches the evolution of the Fermi level ($E = 0$) relative to the midpoint energy $E_{\Gamma\frac{Z}{2}}$ of the cosine band in the EBSs shown in Figures 5 and S8.

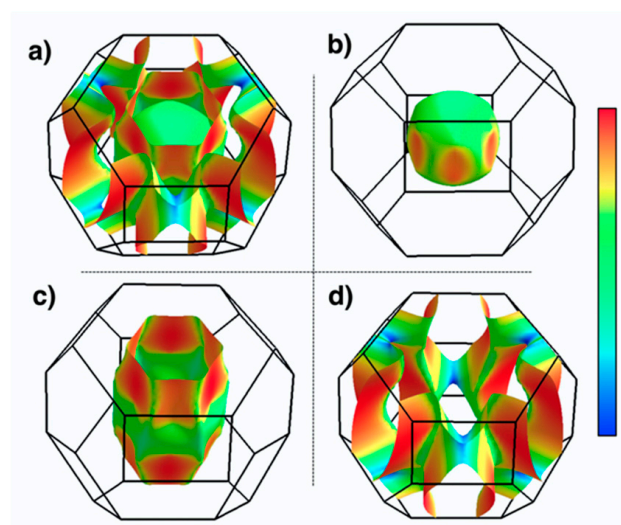


Figure 6. Cont.

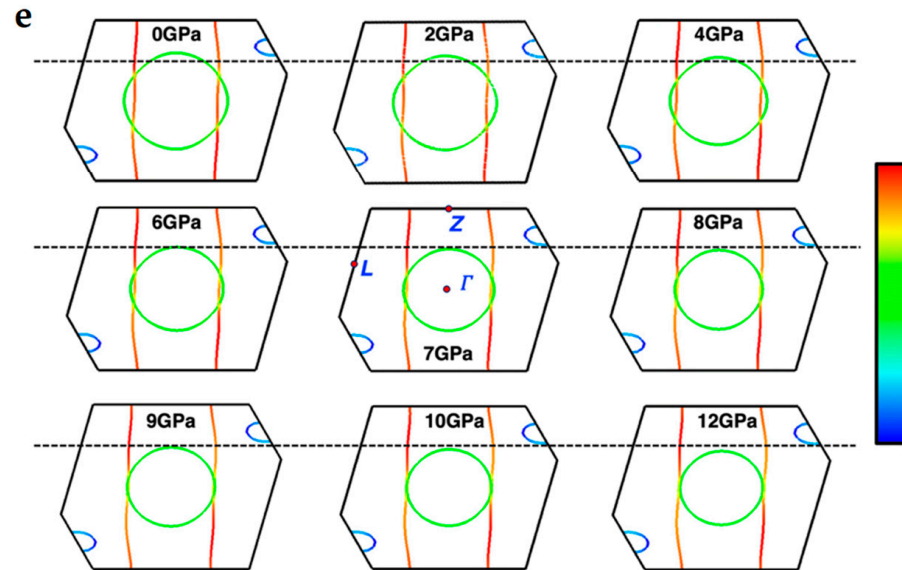


Figure 6. The Fermi surfaces of the rhombohedral unit cell for CaC_6 . (a). The Fermi surfaces of CaC_6 for all bands. (b–d) Individual Fermi surface bands. (e) Cross-sections of FS sections along the $\Gamma - Z - L$ plane (viewed perpendicularly to this plane) as a function of pressure for the rhombohedral primitive unit cell. The colour bar represents the value of the Fermi velocity of electrons. See the text for details.

3.3. Bonding/Antibonding, Superlattice, and Electronic Topological Transitions

Figure 7a–d show the FSs as a function of pressure for the double supercell constructed by the folding procedure of the rhombohedral reciprocal unit cell, as described in Figure 4c. Figure 7e,f (enlarged view of Figure 7e) show the results obtained from calculations at 4 GPa using the double hexagonal supercell (with CASTEP 2023 software). A stack of two adjacent reciprocal unit cells is shown in Figure 7e.

As shown earlier in Figure 4 for 0 GPa, gaps are also generated in the double hexagonal supercell calculation for 4 GPa because of the requirement that bands must intersect BZ boundaries perpendicularly in order to guarantee the continuity of the bands and their derivatives. These FS gap regions relate to the establishment of superconducting gaps, simultaneously with the establishment of key nesting relationships [28,29,57], which link the EBS, the FS, and special phonon vectors from phonon dispersions (PDs). A detailed discussion of such nesting phenomena is provided in a separate companion article [28].

In Figure S10 (Supplement), at approximately 7.5 GPa, there is a notable change in the experimentally determined superconducting transition temperature (T_c) for CaC_6 (see also Figure 5 of reference [28]). This pressure coincides with a significant reduction in the diameter of the almost spherical Ca 4s-orbital FS to the point where the pockets (labelled 0 in Figure 7a,b) just disappear, and pockets (labelled 1 in Figure 7a–d) become disconnected at the BZ boundary. These alterations in the topologies of the FS and the EBS are key to understanding the electronic transport properties of CaC_6 as a function of pressure.

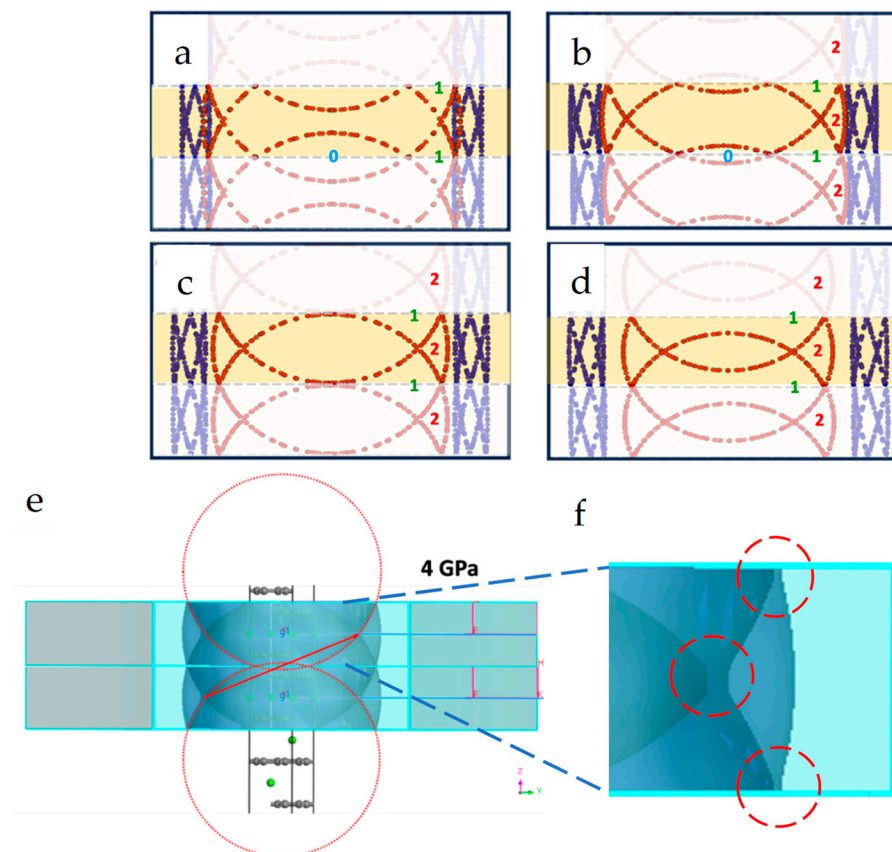


Figure 7. Folded section views of the FS for CaC_6 under (a) 0 GPa, (b) 4 GPa, (c) 7.5 GPa, and (d) 16 GPa. (e) The FS calculated for the $2c$ double hexagonal supercell using CASTEP. Two reciprocal unit cells are displayed together (a single cell is shaded following the scheme of (a–d)). (f) An enlarged view of the intersections with the BZ boundaries. Note that gaps evolve at the boundaries (highlighted inside red dashed-line circles) because of the requirement that bands must be perpendicular to BZ boundary planes (see also Figure 4).

3.3.1. Open and Closed Fermi Surfaces—Topological Transition with Pressure

Open and closed are two types of topologically different FSs [25]. Only closed cross-sections can appear for closed FSs, causing closed trajectories for the movement of electrons in the presence of a magnetic field. In contrast, open FSs can generate both open and closed cross-sections. Figure 8 displays periodically repeated FSs for CaC_6 calculated for the $2c$ double superlattice.

As demonstrated in Figure 7a–f, the FS, characterised by a nearly pure $4s$ orbital nature, extends to the adjacent BZ until the pressure reaches 7.5 GPa, at which point a singularity is observed at the connection point. At 16 GPa, the FS with a pure $4s$ character is confined entirely within the BZ of the double hexagonal supercell. Below 7.5 GPa, the folded FS produces the necking of spherical Fermi regions where continuous domains along the c^* -direction can be identified (see Figure 7a–f).

As the pressure is increased, these spherical regions become disconnected, breaking up what was previously (at lower pressure) an open, interconnected FS path (Figure 7a,b) and transitioning into a closed FS loop (Figure 7c,d; see also Figure 8) [25,58]. We posit that at about 7.5 to 8 GPa, the coupled superlattice delineated nesting relationship that we have proposed [28] moves from the two internal open FSs to two open FSs once the inner FS becomes disconnected and closed, as shown in Figure 8.

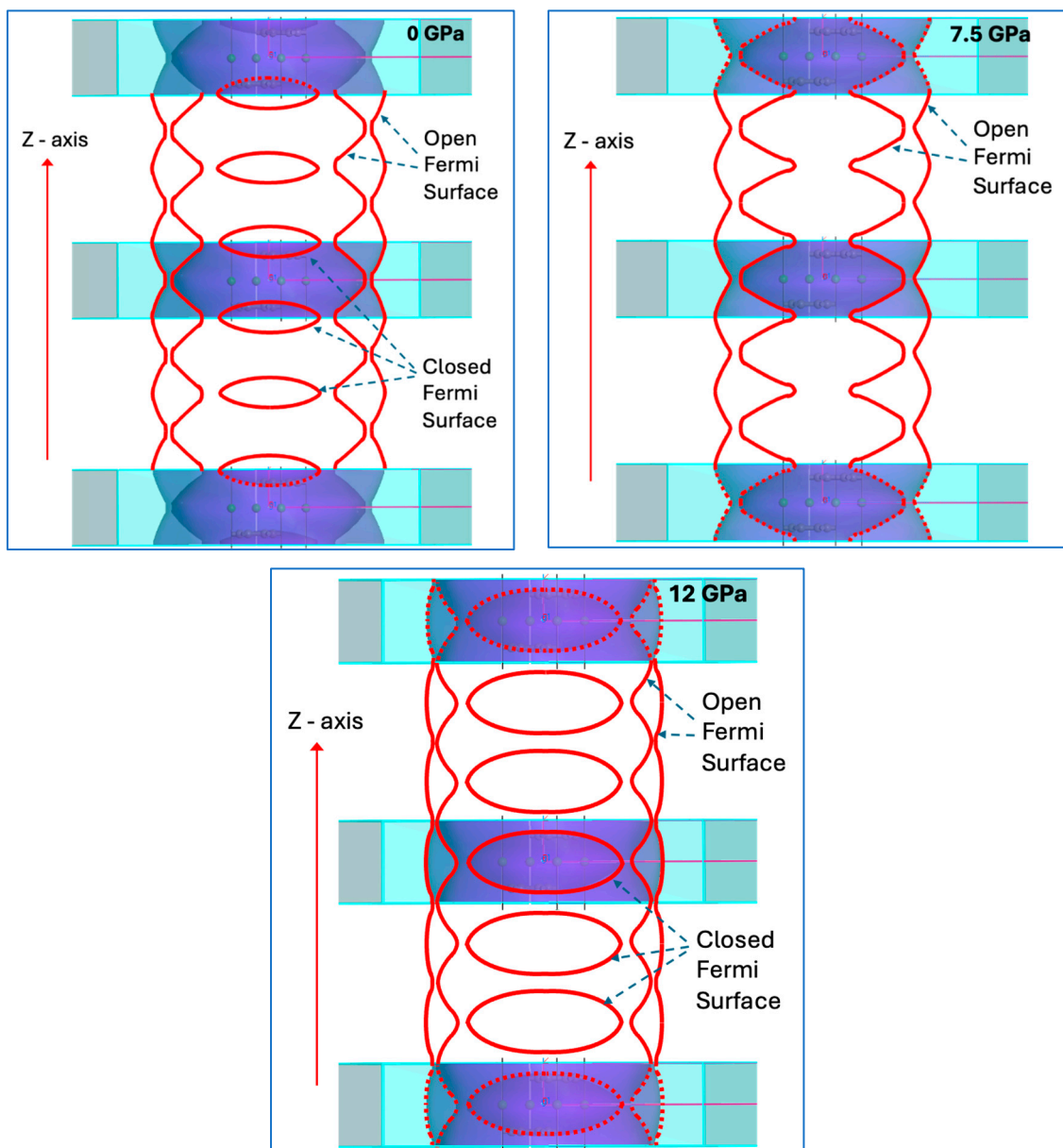


Figure 8. Periodically repeated FSs for CaC_6 calculated for the $2c$ double superlattice at various pressures: 0 GPa, 7.5 GPa, and 12 GPa. Open and closed FSs are labelled. Note that at about 7.5 GPa, the internal open FS is about to become disconnected and closed.

3.3.2. Isoenergetic Fermi Surfaces—Electron Dynamics and Magnetic Fields

The isoenergetic FSs for the $2c$ double hexagonal supercell of CaC_6 at 0 GPa are displayed in Figure 9. These isoenergetic surfaces are closely linked to the dispersion of the electronic bands [25] and play a significant role in understanding electron dynamics. They can be used to determine the effective mass under a magnetic field [25]. Since the experimental determination of superconductivity always requires the exposure of the sample to an external electromagnetic field, either electric for a resistive transition determination, magnetic for a Meissner effect measurement, or electromagnetic via exposure to electromagnetic radiation, at the local level, a range of isoenergetic FSs are always involved.

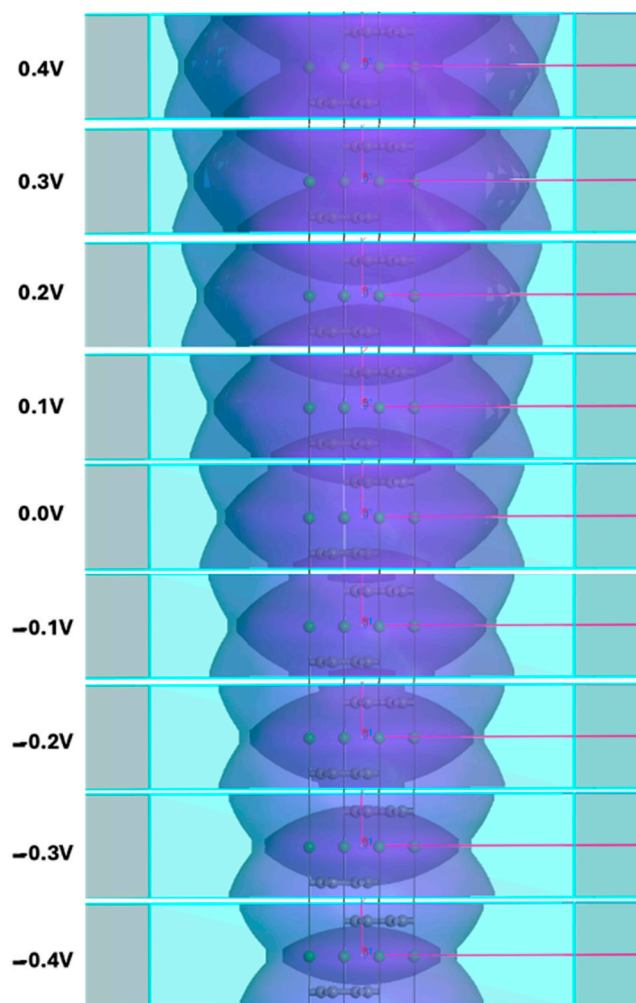


Figure 9. The sequence of isoenergetic FSs for the $2c$ double hexagonal supercell of CaC_6 at 0 GPa. Blue coloured shapes represent shades of the selected FSs. The darker the colour the more overlapping surfaces that are displayed. Isoenergetic values are displayed to the left of the corresponding FS cross-section.

The topological changes described above are often referred to as electronic topological transitions (ETTs) [25,59]. This is a concept that largely evolved from earlier ideas introduced by Lifshitz [25,60]. This concept is typically associated with superconductivity as a function of pressure, as emphasised by Bianconi and colleagues [61–66]. Thus, continuity inside and across the BZ boundaries of interconnected open FS regions for free-electron-like coupled electron transport appears to be a requirement for superconductivity. When these FS regions are open [67], they appear to correlate with the presence of superconductivity. When they are closed, there may be a connection to charge density waves [24].

3.4. Fermi Velocity and Its Connection to the Superconducting Gap

Such FS topological transitions described above, involving shifts from open to closed FSs, or vice versa, particularly under pressure, display a strong resemblance to Lifshitz transitions [68]. These are often associated with changes in T_c and/or even the destruction of superconductivity [61–66]. Figure S10 (Supplemental Materials) is a graph of the experimentally determined superconducting transition temperature (T_c) for CaC_6 , reproduced and adapted from reference [19]. A sharp drop in T_c takes place at about 8 GPa.

The following fundamental relationship is known from the BCS model for superconductivity, where the order parameter or gap energy $\Delta(0)$ is related to the Fermi velocity v_F , the reduced Planck's constant \hbar , and the coherence length $\xi(0)$ [69] as follows:

$$\Delta(0) = \frac{\hbar v_F}{\pi \xi(0)} \quad (5)$$

Different sections of the FSs display clear differences in the Fermi velocity v_F ; therefore, a k -dependent gap energy $\Delta(k)$ anisotropy is expected, and the coherence lengths must be correspondingly different. Based on the colour scale in Figure 6, the Fermi velocity in red areas is about twice the Fermi velocity in green areas. Therefore, coherence length anisotropy is expected and in agreement with experimental results for CaC_6 .

Emery et al. [6] observed different coherence lengths in the ab - and c -directions, ξ_{ab} and ξ_c , of 35 nm and 13 nm, respectively. Since the gradient of the FS determines the main direction of movement of the FS under an external field [25,70], we expect that for the Ca 4s-dominated spherical FS, a shorter coherence length in the c -direction is accessible. For the predominantly C 2p_z-dominated FS, the determined coherence length is predominantly in the ab -direction. Therefore, the green and red FS regions (in terms of Fermi velocities) would have, on average, gaps with a ratio of

$$\frac{(v_F/2)/13}{v_F/35} = \frac{35}{26} = 1.35 \quad (6)$$

Therefore, a change in T_c is expected to be related to the Fano–Feshbach resonance of the gap between different areas of the Fermi surface if, for different reasons, the anisotropy influences a specific measurement or if the dominant FS that determines properties alternates between green and red Fermi velocity regions. Cross-sectional views of the $\Gamma - X - X1$ plane as a function of pressure are displayed in Figure S11 (Supplemental Materials). Figure S11 shows that the Fermi surface exhibits the most hybridised characteristics at a pressure of 7.5 GPa. This hybridisation is likely crucial, as it facilitates the intersection and convolution of the FSs for carbon and calcium, forming what is referred to as intercalant FSs [11,21]. According to Sugawara et al. [21], these intercalant FSs and resultant interlayer bands are essential for the stabilisation of a superconducting state in CaC_6 .

Based on the discussion involving Fermi velocities and coherence lengths above and the discussion on ETT with open or closed FS pockets in Section 3.4, the gap energies can be different in different regions of the FS, in particular, at the Lifshitz transition for “appearing” at a new Fermi surface area and at “opening a neck” topological transitions. The critical temperature shows minima and maxima at the anti-resonance *suppression* and resonance *amplification*, respectively, for pair transfer between different Fermi surface areas [61,62,66,71,72], thus explaining the transition temperature dependence on pressure for CaC_6 near the ETT controlled by the superstructure.

Figure 10 shows the calculated EBS for CaC_6 at 12 GPa using a $2c$ hexagonal supercell and norm-conserving LDA pseudopotential. Figure 10b shows an enlarged view of the higher-energy bands inside the dashed-box inset in Figure 10a. These bands retain approximately the same shape as they extend away from the ΓZ line towards the BZ boundary (see Figure 3 and the discussion in Section 3.1). Furthermore, these bands increase in energy towards the Fermi level as they approach the respective FS in reciprocal space. The dashed circle in Figure 10b identifies an “avoided” band crossing, which should also reflect an FS crossing. We argue that this avoided band crossing limits coherent nesting via acoustic nesting phonons [28]. This avoided band crossing may originate from the computational discreteness of the DFT calculation, which suggests that the separation of crossing bands may decrease if DFT calculations use an even finer Δk -grid than noted above in Section 2.

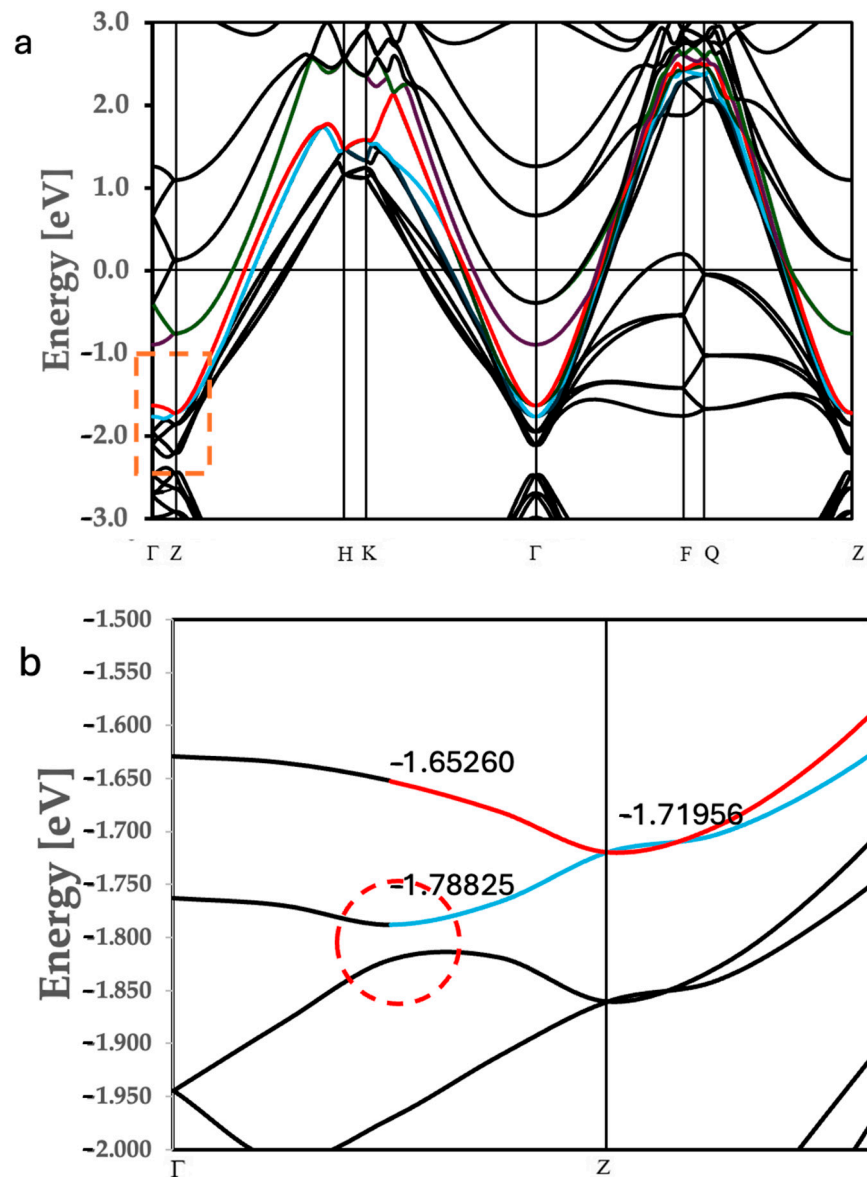


Figure 10. (a) The band structure of CaC_6 at 12 GPa calculated using a $2c$ hexagonal supercell and the LDA pseudopotential and (b) an enlarged view of the region inside the red box in (a). The red box encloses the folded p_z band projections along ΓZ , which become part of the new FS open loops above an ETT pressure of about 7.5 GPa. The blue and red bands indicate bonding and antibonding sections of the band. The dashed circle highlights an “avoided” crossing of bands, which we suggest destroys the coherent coupling of bonding and antibonding electrons.

However, there may exist quantum mechanical and/or symmetry conditions that lead to the avoided band crossing. For example, the approximate energies of the split bonding/antibonding p_z band close to the avoided crossing are labelled in Figure 10b. The energy values are -1.652603 eV for the high-energy antibonding end and -1.788252 eV for the low-energy bonding end, with an average of -1.720427 eV. The nonbonding energy is -1.71956 eV. Therefore, the asymmetry is $|-0.000867 \text{ eV}| = 0.87 \text{ meV}$. Remarkably, this asymmetry is comparable to half the superconducting gap energy of 1.7 meV for CaC_6 at 0 GPa [17,28] and corresponds to approximately half the T_c , or $11.4 \text{ K}/2 = 5.7 \text{ K}$. This value is close to the experimental T_c value previously measured for CaC_6 at this pressure (see Figure S10). Note that these values are approaching the limit of the effective resolution for DFT calculations with the computational parameter choices described in Methods.

A careful inspection of Figure 3a and a comparison to Figure 10a show that the p_z bands in Figure 3a cross with a wider gap in energy and farther away from the inflection point of the cosine band. The asymmetry of the bonding/antibonding bands at 0 GPa is larger in energy (estimated at ~ 1.5 meV) and covers a wider extent of the reciprocal ΓZ direction (from the Z point). This condition at 0 GPa translates into a greater extent of nesting [28]. This nested region provides a parallel channel of lower gap energy than the Ca-4s bands at lower pressures. If the extent of crossing for p_z bands from the Z point is reduced at an approximately linear rate with pressure, then the 12 GPa values given above suggest that, at 24 GPa, superconductivity may be completely destroyed.

4. Conclusions

A comprehensive analysis of the electronic properties of CaC_6 under varying pressures has been presented. Using DFT calculations, we have investigated the evolution of topologies for the Fermi surface and electronic band structures of CaC_6 . The Fermi surface of CaC_6 consists of three bands, with two of these bands intersecting and gradually decoupling with increasing pressure. This evolution of the FS is concurrent with a sharp drop in superconducting properties, indicating a strong correlation between FS and EBS topologies and superconductivity in CaC_6 .

Our analysis reveals that the highest T_c for superconductivity in CaC_6 occurs when the cosine-shaped interlayer band is half-filled. Folding the FS and EBS at the midpoint of this characteristic cosine-shaped band by introducing a $2c$ supercell (producing a halving of the rhombohedral c^* -direction), the FS of the double superlattice defines interconnected pockets, or open loops, which are favourable for nearly free electron coupled movement and superconductivity when the pressure is below 7.5 GPa. At pressures above 8 GPa, the original FS pockets become disconnected and transform into closed loops, manifesting substantial changes in superconducting properties.

By invoking a superlattice perspective of material properties, motivated by the bonding/antibonding character encapsulated in the cosine-modulated electronic band, we not only clarify the bonding/antibonding interaction but also uncover a Lifshitz or electronic topological transition with significant implications for electronic properties with changes in external conditions such as pressure. This analysis brings the pressure behaviour and characteristics of CaC_6 in line with those of many other layered and non-layered superconductors based on key fundamental principles and mechanisms that influence superconducting properties.

Our study enhances our understanding of the pressure-dependent electronic properties of CaC_6 and offers insight into the mechanisms that control the critical temperature for superconductivity in this compound. The findings not only advance our knowledge of superconductivity in graphite intercalation compounds by identifying important EBS and FS characteristics as requirements for superconductivity but also open potential new paths for optimising the anisotropic superconducting gap in graphite intercalated compounds and for exploring novel materials with improved superconducting properties under pressure.

Supplementary Materials: The following supporting information can be downloaded at <https://www.mdpi.com/article/10.3390/cryst14060554/s1>: Figure S1: Structures of unit cells before and after relaxation; Figure S2: DFT parameters for CaC_6 ; Figure S3: K-point mesh grid and Fermi energy; Figure S4: Pseudopotentials and change in lattice constants; Figure S5: High-symmetry conventions; Figure S6: Projected energy bands and DOS for rhombohedral primitive cell; Figure S7: Schematic of FS $\Gamma - Z - L$ directions at 2 GPa; Figure S8: EBS along ΓZ for primitive cell with pressure; Figure S9: Fermi surfaces for rhombohedral unit cell as a function of pressure; Figure S10: Experimental T_c with pressure for CaC_6 ; Figure S11: Orbital character of FS with pressure; Table S1: Properties of CaC_6 with pressure.

Author Contributions: Conceptualisation, J.A.A. and I.D.R.M.; methodology, B.W., A.B. and J.A.A.; software, B.W. and J.A.A.; validation, J.A.A., I.D.R.M. and A.B.; formal analysis, J.A.A., A.B. and I.D.R.M.; investigation, B.W.; resources, J.A.A.; writing—original draft preparation, B.W. and J.A.A.;

writing—review and editing, J.A.A. and I.D.R.M.; visualisation, I.D.R.M. and J.A.A.; supervision, J.A.A. All authors have read and agreed to the published version of the manuscript.

Funding: This research received no external funding.

Data Availability Statement: The raw data supporting the conclusions of this article will be made available by the authors on request.

Acknowledgments: We extend our gratitude to QUT for a scholarship award to BW and access to high-performance computing (HPC), and to Craig Windell, Jakub Szarlat, and Vicki Thomson and the Research team for their assistance with HPC facilities. Our appreciation also goes to The University of Queensland's Research Computing Centre (RCC) for its invaluable support in this research, with a special mention to Marlies Hankel for her persistence.

Conflicts of Interest: The authors declare no conflicts of interest.

References

1. Jishi, R.A.; Dresselhaus, M.S. Superconductivity in graphite intercalation compounds. *Phys. Rev. B* **1992**, *45*, 12465–12469. [[CrossRef](#)] [[PubMed](#)]
2. Hannay, N.B.; Geballe, T.H.; Matthias, B.T.; Andres, K.; Schmidt, P.; MacNair, D. Superconductivity in Graphitic Compounds. *Phys. Rev. Lett.* **1965**, *14*, 225–226. [[CrossRef](#)]
3. Smith, R.P.; Weller, T.E.; Howard, C.A.; Dean, M.P.M.; Rahnejat, K.C.; Saxena, S.S.; Ellerby, M. Superconductivity in graphite intercalation compounds. *Phys. C Supercond. Appl.* **2015**, *514*, 50–58. [[CrossRef](#)]
4. Weller, T.E.; Ellerby, M.; Saxena, S.S.; Smith, R.P.; Skipper, N.T. Superconductivity in the intercalated graphite compounds C_6Yb and C_6Ca . *Nat. Phys.* **2005**, *1*, 39–41. [[CrossRef](#)]
5. Mazin, I.I. Intercalant-Driven Superconductivity in YbC_6 and CaC_6 . *Phys. Rev. Lett.* **2005**, *95*, 227001. [[CrossRef](#)] [[PubMed](#)]
6. Emery, N.; Hérold, C.; d'Astuto, M.; Garcia, V.; Bellin, C.; Marêché, J.F.; Lagrange, P.; Loupiau, G. Superconductivity of Bulk CaC_6 . *Phys. Rev. Lett.* **2005**, *95*, 087003. [[CrossRef](#)] [[PubMed](#)]
7. Kanetani, K.; Sugawara, K.; Sato, T.; Shimizu, R.; Iwaya, K.; Hitosugi, T.; Takahashi, T. Ca intercalated bilayer graphene as a thinnest limit of superconducting C_6Ca . *Proc. Natl. Acad. Sci. USA* **2012**, *109*, 19610–19613. [[CrossRef](#)] [[PubMed](#)]
8. Ichinokura, S.; Sugawara, K.; Takayama, A.; Takahashi, T.; Hasegawa, S. Superconducting Calcium-Intercalated Bilayer Graphene. *ACS Nano* **2016**, *10*, 2761–2765. [[CrossRef](#)] [[PubMed](#)]
9. Cao, Y.; Fatemi, V.; Fang, S.; Watanabe, K.; Taniguchi, T.; Kaxiras, E.; Jarillo-Herrero, P. Unconventional superconductivity in magic-angle graphene superlattices. *Nature* **2018**, *556*, 43–50. [[CrossRef](#)] [[PubMed](#)]
10. Csányi, G.; Littlewood, P.B.; Nevidomskyy, A.H.; Pickard, C.J.; Simons, B.D. The role of the interlayer state in the electronic structure of superconducting graphite intercalated compounds. *Nat. Phys.* **2005**, *1*, 42–45. [[CrossRef](#)]
11. Calandra, M.; Mauri, F. Theoretical Explanation of Superconductivity in CaC_6 . *Phys. Rev. Lett.* **2005**, *95*, 237002. [[CrossRef](#)] [[PubMed](#)]
12. McMillan, W.L. Transition Temperature of Strong-Coupled Superconductors. *Phys. Rev.* **1968**, *167*, 331–344. [[CrossRef](#)]
13. Hinks, D.G.; Rosenmann, D.; Claus, H.; Bailey, M.S.; Jorgensen, J.D. Large Ca isotope effect in the CaC_6 superconductor. *Phys. Rev. B* **2007**, *75*, 014509. [[CrossRef](#)]
14. Lamura, G.; Aurino, M.; Cifariello, G.; Di Gennaro, E.; Andreone, A.; Emery, N.; Hérold, C.; Marêché, J.F.; Lagrange, P. Experimental Evidence of s-Wave Superconductivity in Bulk CaC_6 . *Phys. Rev. Lett.* **2006**, *96*, 107008. [[CrossRef](#)] [[PubMed](#)]
15. Bergeal, N.; Dubost, V.; Noat, Y.; Sacks, W.; Roditchev, D.; Emery, N.; Hérold, C.; Marêché, J.F.; Lagrange, P.; Loupiau, G. Scanning Tunneling Spectroscopy on the Novel Superconductor CaC_6 . *Phys. Rev. Lett.* **2006**, *97*, 077003. [[CrossRef](#)] [[PubMed](#)]
16. Sanna, A.; Profeta, G.; Floris, A.; Marini, A.; Gross, E.K.U.; Massidda, S. Anisotropic gap of superconducting CaC_6 : A first-principles density functional calculation. *Phys. Rev. B* **2007**, *75*, 020511. [[CrossRef](#)]
17. Gonnelli, R.S.; Daghero, D.; Delaude, D.; Tortello, M.; Ummerino, G.A.; Stepanov, V.A.; Kim, J.S.; Kremer, R.K.; Sanna, A.; Profeta, G.; et al. Evidence for Gap Anisotropy in CaC_6 from Directional Point-Contact Spectroscopy. *Phys. Rev. Lett.* **2008**, *100*, 207004. [[CrossRef](#)]
18. Smith, R.P.; Kusmartseva, A.; Ko, Y.T.C.; Saxena, S.S.; Akrap, A.; Forró, L.; Laad, M.; Weller, T.E.; Ellerby, M.; Skipper, N.T. Pressure dependence of the superconducting transition temperature in C_6Yb and C_6Ca . *Phys. Rev. B* **2006**, *74*, 024505. [[CrossRef](#)]
19. Gauzzi, A.; Takashima, S.; Takeshita, N.; Terakura, C.; Takagi, H.; Emery, N.; Hérold, C.; Lagrange, P.; Loupiau, G. Enhancement of Superconductivity and Evidence of Structural Instability in Intercalated Graphite CaC_6 under High Pressure. *Phys. Rev. Lett.* **2007**, *98*, 067002. [[CrossRef](#)] [[PubMed](#)]
20. Gauzzi, A.; Bendiab, N.; d'Astuto, M.; Canny, B.; Calandra, M.; Mauri, F.; Loupiau, G.; Emery, N.; Hérold, C.; Lagrange, P.; et al. Maximum T_c at the verge of a simultaneous order-disorder and lattice-softening transition in superconducting CaC_6 . *Phys. Rev. B* **2008**, *78*, 064506. [[CrossRef](#)]
21. Sugawara, K.; Sato, T.; Takahashi, T. Fermi-surface-dependent superconducting gap in C_6Ca . *Nat. Phys.* **2009**, *5*, 40–43. [[CrossRef](#)]
22. Valla, T.; Pan, Z. Superconductivity and Electron-Phonon Coupling in Graphite Intercalation Compounds. In *Physics and Applications of Graphene-Experiments*; IntechOpen: London, UK, 2011.

23. Yang, S.L.; Sobota, J.A.; Howard, C.A.; Pickard, C.J.; Hashimoto, M.; Lu, D.H.; Mo, S.K.; Kirchmann, P.S.; Shen, Z.X. Superconducting graphene sheets in CaC_6 enabled by phonon-mediated interband interactions. *Nat. Commun.* **2014**, *5*, 3493. [[CrossRef](#)] [[PubMed](#)]
24. Rahnejat, K.C.; Howard, C.A.; Shuttleworth, N.E.; Schofield, S.R.; Iwaya, K.; Hirjibehedin, C.F.; Renner, C.; Aeppli, G.; Ellerby, M. Charge density waves in the graphene sheets of the superconductor CaC_6 . *Nat. Commun.* **2011**, *2*, 558. [[CrossRef](#)] [[PubMed](#)]
25. Kosevich, A.M. Topology in the Theory of Metals. In *Topology in Condensed Matter*; Monastyrsky, M.I., Ed.; Springer Science & Business Media: Berlin/Heidelberg, Germany, 2006; Volume 150.
26. Rezende, S.M. *Introduction to Electronic Materials and Devices*; Springer Nature: Berlin/Heidelberg, Germany, 2022.
27. Moessner, R.; Moore, J.E. *Topological Phases of Matter*; Cambridge University Press: Cambridge, UK, 2021.
28. Wang, B.; Bianconi, A.; Mackinnon, I.D.R.; Alarco, J.A. Superlattice delineated Fermi surface nesting and electron-phonon coupling in CaC_6 . *Crystals* **2024**, *14*, 499. [[CrossRef](#)]
29. Alarco, J.A.; Mackinnon, I.D.R. Superlattices, Bonding-Antibonding, Fermi Surface Nesting, and Superconductivity. *Condens. Matter* **2023**, *8*, 72. [[CrossRef](#)]
30. Giannozzi, P.; Baroni, S.; Bonini, N.; Calandra, M.; Car, R.; Cavazzoni, C.; Ceresoli, D.; Chiarotti, G.L.; Cococcioni, M.; Dabo, I.; et al. QUANTUM ESPRESSO: A modular and open-source software project for quantum simulations of materials. *J. Phys. Condens. Matter* **2009**, *21*, 395502. [[CrossRef](#)] [[PubMed](#)]
31. Clark, S.J.; Segall, M.D.; Pickard, C.J.; Hasnip, P.J.; Probert, M.I.J.; Refson, K.; Payne, M.C. First principles methods using CASTEP. *Z. Kristallogr. Cryst. Mater.* **2005**, *220*, 567–570. [[CrossRef](#)]
32. Mackinnon, I.D.R.; Almutairi, A.; Alarco, J.A. Insights from Systematic DFT Calculations on Superconductors. In *Real Perspective of Fourier Transforms and Current Developments in Superconductivity*; Arcos, J.M.V., Ed.; IntechOpen: London, UK, 2021; pp. 1–29.
33. Alarco, J.A.; Almutairi, A.; Mackinnon, I.D.R. Progress towards a Universal Approach for Prediction of the Superconducting Transition Temperature. *J. Supercond. Nov. Magn.* **2020**, *33*, 2287–2292. [[CrossRef](#)]
34. Alarco, J.A.; Talbot, P.C.; Mackinnon, I.D.R. Identification of superconductivity mechanisms and prediction of new materials using Density Functional Theory (DFT) calculations. *J. Phys. Conf. Ser.* **2018**, *1143*, 012028. [[CrossRef](#)]
35. Sabatini, R.; Küçükbenli, E.; Pham, C.H.; De Gironcoli, S. Phonons in nonlocal van der Waals density functional theory. *Phys. Rev. B* **2016**, *93*, 235120. [[CrossRef](#)]
36. Berland, K.; Londero, E.; Schröder, E.; Hyldgaard, P. Harris-type van der Waals density functional scheme. *Phys. Rev. B* **2013**, *88*, 045431. [[CrossRef](#)]
37. Hyldgaard, P.; Jiao, Y.; Shukla, V. Screening nature of the van der Waals density functional method: A review and analysis of the many-body physics foundation. *J. Phys. Condens. Matter* **2020**, *32*, 393001. [[CrossRef](#)] [[PubMed](#)]
38. Lee, K.; Murray, É.D.; Kong, L.; Lundqvist, B.I.; Langreth, D.C. Higher-accuracy van der Waals density functional. *Phys. Rev. B* **2010**, *82*, 081101. [[CrossRef](#)]
39. Chakraborty, D.; Berland, K.; Thonhauser, T. Next-Generation Nonlocal van der Waals Density Functional. *J. Chem. Theory Comput.* **2020**, *16*, 5893–5911. [[CrossRef](#)] [[PubMed](#)]
40. Berland, K.; Chakraborty, D.; Thonhauser, T. van der Waals density functional with corrected C_6 coefficients. *Phys. Rev. B* **2019**, *99*, 195418. [[CrossRef](#)]
41. Kawaguchi, N.; Shibata, K.; Mizoguchi, T. Possible New Graphite Intercalation Compounds for Superconductors and Charge Density Wave Materials: Systematic Simulations with Various Intercalants Using a van der Waals Density Functional Method. *J. Phys. Chem. C* **2023**, *127*, 9833–9843. [[CrossRef](#)]
42. Alarco, J.A.; Talbot, P.C.; Mackinnon, I.D.R. Comparison of Functionals for Metal Hexaboride Band Structure Calculations. *Model. Numer. Simul. Mater. Sci.* **2014**, *4*, 53–69. [[CrossRef](#)]
43. Alarco, J.A.; Chou, A.; Talbot, P.C.; Mackinnon, I.D.R. Phonon Modes of MgB_2 : Super-lattice Structures and Spectral Response. *Phys. Chem. Chem. Phys.* **2014**, *16*, 24443–24456. [[CrossRef](#)] [[PubMed](#)]
44. Alarco, J.A.; Talbot, P.C.; Mackinnon, I.D.R. Coherent phonon decay and the boron isotope effect for MgB_2 . *Phys. Chem. Chem. Phys.* **2014**, *16*, 25386–25392. [[CrossRef](#)] [[PubMed](#)]
45. Bartók, A.P.; Yates, J.R. Ultrasoft pseudopotentials with kinetic energy density support: Implementing the Tran-Blaha potential. *Phys. Rev. B* **2019**, *99*, 235103. [[CrossRef](#)]
46. Perdew, J.P.; Burke, K.; Ernzerhof, M. Generalized Gradient Approximation Made Simple. *Phys. Rev. Lett.* **1996**, *77*, 3865–3868. [[CrossRef](#)]
47. Perdew, J.P.; Chevary, J.A.; Vosko, S.H.; Jackson, K.A.; Pederson, M.R.; Singh, D.J.; Fiolhais, C. Atoms, molecules, solids, and surfaces: Applications of the generalized gradient approximation for exchange and correlation. *Phys. Rev. B* **1992**, *46*, 6671–6687. [[CrossRef](#)] [[PubMed](#)]
48. Monkhorst, H.J.; Pack, J.D. Special points for Brillouin-zone integrations. *Phys. Rev. B* **1976**, *13*, 5188–5192. [[CrossRef](#)]
49. Marzari, N.; Vanderbilt, D.; De Vita, A.; Payne, M.C. Thermal Contraction and Disordering of the Al(110) Surface. *Phys. Rev. Lett.* **1999**, *82*, 3296–3299. [[CrossRef](#)]
50. Setyawan, W.; Curtarolo, S. High-throughput electronic band structure calculations: Challenges and tools. *Comput. Mater. Sci.* **2010**, *49*, 299–312. [[CrossRef](#)]
51. Harrison, W.A. *Applied Quantum Mechanics*; World Scientific: Singapore, 2000.

52. Kawamura, M. FermiSurfer: Fermi-surface viewer providing multiple representation schemes. *Comput. Phys. Commun.* **2019**, *239*, 197–203. [[CrossRef](#)]
53. Sanville, E.; Kenny, S.D.; Smith, R.; Henkelman, G. Improved grid-based algorithm for Bader charge allocation. *J. Comput. Chem.* **2007**, *28*, 899–908. [[CrossRef](#)]
54. Tang, W.; Sanville, E.; Henkelman, G. A grid-based Bader analysis algorithm without lattice bias. *J. Phys. Condens. Matter* **2009**, *21*, 084204. [[CrossRef](#)] [[PubMed](#)]
55. Yu, M.; Trinkle, D.R. Accurate and efficient algorithm for Bader charge integration. *J. Chem. Phys.* **2011**, *134*, 064111. [[CrossRef](#)] [[PubMed](#)]
56. Henkelman, G.; Arnaldsson, A.; Jónsson, H. A fast and robust algorithm for Bader decomposition of charge density. *Comput. Mater. Sci.* **2006**, *36*, 354–360. [[CrossRef](#)]
57. Alarco, J.A.; Gupta, B.; Shahbazi, M.; Appadoo, D.; Mackinnon, I.D.R. THz/Far infrared synchrotron observations of superlattice frequencies in MgB₂. *Phys. Chem. Chem. Phys.* **2021**, *23*, 23922–23932. [[CrossRef](#)] [[PubMed](#)]
58. Mazziotti, M.V.; Raimondi, R.; Valletta, A.; Campi, G.; Bianconi, A. Resonant multi-gap superconductivity at room temperature near a Lifshitz topological transition in sulfur hydrides. *J. Appl. Phys.* **2021**, *130*, 173904. [[CrossRef](#)]
59. Blanter, Y.M.; Kaganov, M.I.; Pantsulaya, A.V.; Varlamov, A.A. The theory of electronic topological transitions. *Phys. Rep.* **1994**, *245*, 159–257. [[CrossRef](#)]
60. Lifshitz, I.M.; Kaganov, M.I. Geometrical concepts in the Electron Theory of Metals. In *Electrons at the Fermi Surface*; Springfield, M., Ed.; Cambridge University Press: Cambridge, UK, 2011.
61. Bianconi, A. Lifshitz Transitions in Multi-band Hubbard Models for Topological Superconductivity in Complex Quantum Matter. *J. Supercond. Nov. Magn.* **2018**, *31*, 603–610. [[CrossRef](#)]
62. Mazziotti, M.V.; Bianconi, A.; Raimondi, R.; Campi, G.; Valletta, A. Spin-orbit coupling controlling the superconducting dome of artificial superlattices of quantum wells. *arXiv* **2022**, arXiv:2211.11547. [[CrossRef](#)]
63. Angilella, G.G.N.; Bianconi, A.; Pucci, R. Multiband Superconductors Close to a 3D–2D Electronic Topological Transition. *J. Supercond.* **2005**, *18*, 619–623. [[CrossRef](#)]
64. Jarlborg, T.; Bianconi, A. Breakdown of the Migdal approximation at Lifshitz transitions with giant zero-point motion in the H₃S superconductor. *Sci. Rep.* **2016**, *6*, 24816. [[CrossRef](#)] [[PubMed](#)]
65. Simonelli, L.; Palmisano, V.; Fratini, M.; Filippi, M.; Parisiades, P.; Lampakis, D.; Liarokapis, E.; Bianconi, A. Isotope effect on the E_{2g} phonon and mesoscopic phase separation near the electronic topological transition in Mg_{1-x}Al_xB₂. *Phys. Rev. B Condens. Matter Mater. Phys.* **2009**, *80*, 14520. [[CrossRef](#)]
66. Agrestini, S.; Metallo, C.; Filippi, M.; Simonelli, L.; Campi, G.; Sanipoli, C.; Liarokapis, E.; De Negri, S.; Giovannini, M.; Saccone, A.; et al. Substitution of Sc for Mg in MgB₂: Effects on transition temperature and Kohn anomaly. *Phys. Rev. B* **2004**, *70*, 134514. [[CrossRef](#)]
67. Brandt, N.B.; Chudinov, S.M. *Electronic Structure of Metals*; Revised from the 1973 Russian ed.; Mir: Moscow, Russia, 1975.
68. Lifshitz, I.M. Anomalies of Electron Characteristics in the High Pressure Region. *Sov. Phys. JETP* **1960**, *11*, 1130–1135.
69. Tinkham, M. *Introduction to Superconductivity*, 2nd ed.; Dover Publications: Mineola, NY, USA, 2004.
70. Alarco, J.A.; Shahbazi, M.; Mackinnon, I.D.R. Experimental control of T_c in AlB₂-type compounds using an applied voltage. *arXiv* **2022**, arXiv:2204.00151.
71. Bianconi, A. Feshbach shape resonance in multiband superconductivity in heterostructures. *J. Supercond.* **2005**, *18*, 626–636. [[CrossRef](#)]
72. Tajima, H.; Aoki, H.; Perali, A.; Bianconi, A. Emergent Fano-Feshbach resonance in two-band superconductors with an incipient quasiflat band: Enhanced critical temperature evading particle-hole fluctuations. *Phys. Rev. B* **2024**, *109*, L140504. [[CrossRef](#)]

Disclaimer/Publisher's Note: The statements, opinions and data contained in all publications are solely those of the individual author(s) and contributor(s) and not of MDPI and/or the editor(s). MDPI and/or the editor(s) disclaim responsibility for any injury to people or property resulting from any ideas, methods, instructions or products referred to in the content.